Fermi surface of $2H$-NbSe$_2$ and its implications on the charge-density-wave mechanism

K. Rossnagel, O. Seifarth, L. Kipp, and M. Skibowski
Institut für Experimentelle und Angewandte Physik, Universität Kiel, D–24098 Kiel, Germany

D. Voß, P. Krüger, A. Mazur, and J. Pollmann
Institut für Festkörpertheorie, Universität Münster, D-48149 Münster, Germany

We report a detailed experimental and theoretical investigation of the Fermi-surface topology of the layered transition-metal dichalcogenide $2H$-NbSe$_2$, which undergoes a second-order phase transition into an incommensurate two-dimensional charge-density-wave phase at 33.5 K. High-resolution angle-resolved photoemission with synchrotron radiation yields two Nb $4d$-related Fermi-surface cylinders and a Se $4p_z$-derived pocket around the center of the Brillouin zone, in good agreement with the results of fully relativistic *ab initio* calculations within the local-density approximation of density-functional theory. The measurements were carried out at 50 K to identify characteristic features in the electronic structure of the normal phase that can give important clues as to the origins of the phase transition, and to achieve high resolution, at the same time. The implications of our results on the charge-density-wave mechanism in $2H$-NbSe$_2$ are discussed. Our results together with previous data from the literature seem to rule out the saddle-point mechanism, but they reveal at the same time that the driving mechanism for the transition into the charge-density-wave state is *not* a simple Fermi-surface nesting, as recently suggested by Straub *et al.* [Phys. Rev. Lett. **82**, 4504 (1999)].

PACS number(s): 71.18.+y, 71.45.Lr, 79.60.−i

I. INTRODUCTION

Layered transition-metal dichalcogenides (TMDC's) provide a fascinating field of structural phase transitions that are associated with charge-density waves (CDW's), i.e., they directly show effects of coupling between electrons and phonons. Among the many TMDC's with CDW instabilities, $2H$-NbSe$_2$ has attracted particular attention because of the coexistence and possible interaction of the CDW and a superconducting phase.[1,2] So far, however, a conclusive picture of the topology of the three-dimensional Fermi surface (FS) and its relation to the observed CDW has not yet been achieved.

As first revealed by neutron scattering, the quasi-two-dimensional layer compound $2H$-NbSe$_2$ undergoes a second-order phase transition to an incommensurate CDW phase at $T_{CDW} = 33.5$ K.[3] The three equivalent CDW wave vectors of the hexagonal Brillouin zone (BZ) are aligned parallel to the ΓM directions, and have a magnitude of $\frac{2}{3}|\Gamma M|(1-\delta)$, with $\delta \approx 0.02$ being slightly temperature dependent. Thus the incommensurability amounts to 2% only. The resistivity shows only a 5% anomaly at T_{CDW}, and remains metallic below.[4] In addition to the CDW phase, $2H$-NbSe$_2$ exhibits a coexisting superconducting phase at and below $T_C = 7.2$ K.[5]

Although it seems to be clear that the origin of the CDW instability in $2H$-NbSe$_2$ (and other TMDC's) is intimately related to their electronic structure close to the Fermi level, experimental information on the FS is rather scarce. De Haas–van Alphen (dHvA) experiments[6,7] have successfully detected a small pancake-shaped FS originating from a $k_\perp$ dispersive Se $4p_z$-related band in the center of the BZ in accordance with recent density functional calculations,[7,8] including the one presented in this work. But no dHvA signal has ever been observed for the two cylindrical Nb $4d$-derived surfaces centered at the ΓA and KH lines of the

BZ, both of which were already predicted by early non-self-consistent band calculations.[9,10] The first experimental evidence of one of these two cylindrical FS sheets (the one at ΓA) came from electron-positron annihilation.[11] The existence of both of these was not confirmed until recently, when an image of a two-dimensional FS cross section at one specific $k_\perp$ value was reported by Straub *et al.*[8] on the basis of an angle-resolved photoelectron spectroscopy (ARPES) study. In spite of these efforts, an experimental determination of the $k_\perp$ dependence of all three FS sheets, which might be essential for a detailed understanding of the CDW instability, is still lacking.

The mechanism responsible for the CDW transition in the $2H$ family of the TMDC's is a matter of ongoing debate. Based on band theoretical results,[9,10] two different origins of the CDW instability have been proposed: the FS nesting mechanism,[12–14] being similar in nature to a Peierls transition of one-dimensional metals, and the saddle-point mechanism, as suggested by Rice and Scott.[15] In the first case the observed wave vector of the CDW spans large parallel sections of the FS; in the latter, the CDW vector is given by the **k**-space separation of two saddle points in the electronic structure close to the Fermi level. Recently, Straub *et al.*[8] strongly favored the FS nesting mechanism for $2H$-NbSe$_2$. But only self-nesting of the ΓA-centered FS was considered in this study, completely ignoring any $k_\perp$ dependence of this sheet, and the question of whether there is any gap at the nested FS was not addressed.

To contribute to a more basic understanding of important physical properties of the intriguing class of $2H$ TMDC's, we have carried out a detailed experimental and theoretical study of the three-dimensional FS of $2H$-NbSe$_2$. Employing ARPES at various photon energies, we have mapped all FS sheets predicted by band-structure calculations in a single experiment. We find that the measured FS sheets are in good

agreement with our density-functional calculation results. On the basis of our findings we cannot confirm that the driving mechanism for the CDW instability is as simple as the common Fermi-surface nesting.

II. EXPERIMENT AND THEORY

The $2H$-NbSe$_2$ crystals were grown by chemical vapor transport, using iodine as the transport gas, and clean surfaces were prepared by cleaving the samples in ultrahigh vacuum. ARPES measurements were carried out at beamline W3.2 at the Hamburger Synchrotronstrahlungslabor (HASYLAB). The incident photons were linearly polarized with the photon polarization and the plane of incidence both residing in the horizontal plane. Photoemission spectra were taken with our recently developed spectrometer ASPHERE (angular spectrometer for photoelectrons with high-energy resolution)[16] which consists of a 100-mm radius hemispherical deflection analyzer mounted on a two-axis goniometer. Computer-controlled stepper motors enable sequential angle scanned measurements with an absolute angular precision of better than 0.1°. The angular acceptance, which can be adjusted by means of an iris aperture, was set to 1°. The combined (electron and photon) energy resolution was 60 meV, and the Fermi-level reference was obtained from a polycrystalline gold film which was in electrical contact with the sample.

Fully relativistic *ab initio* band structure calculations were carried out employing density-functional theory within the local-density approximation.[17] We have used the norm-conserving, nonlocal pseudopotentials of Bachelet, Hamann, and Schlüter.[18] The exchange-correlation energy was taken into account using the Ceperley-Alder[19] form as parametrized by Perdew and Zunger.[20] As a basis set to represent the wave functions, we employ 200 Gaussian orbitals of s, p, d, and s^* symmetry per unit cell and spin. These orbitals are localized at the atomic positions, namely, 40 at each Nb and 30 at each Se atom. The decay constants of the Gaussians are {0.17, 0.45, 1.18, 2.00} for Nb and {0.17, 0.45, 1.00} for Se (in atomic units). A linear mesh of about 0.18 Å in real space is used for the representation of the charge density and the potential. Spin-orbit interaction is considered in each step of the iteration. It is treated in an on-site approximation, i.e., only integrals with the same location of the Gaussian orbitals and the spin-orbit potential are taken into account. The lattice parameters used in the calculations are $a=3.45$ Å, $c=12.54$ Å, and $z=0.134c$.

Figure 1 shows the theoretical band structure from 6 eV below to 3 eV above the Fermi level along various high-symmetry directions in the BZ. The overall disposition of Nb $4d$ and Se $4p$ dominant bands is in good correspondence with the calculation presented in Ref. 7. In particular, the Fermi surface is produced by *three* bands: two Nb $4d$-derived bands and a band of Se $4p$ character around the Γ point.

III. FERMI SURFACE

In Fig. 2 we present our results on the normal phase FS of $2H$-NbSe$_2$. The ARPES data were taken at a temperature of
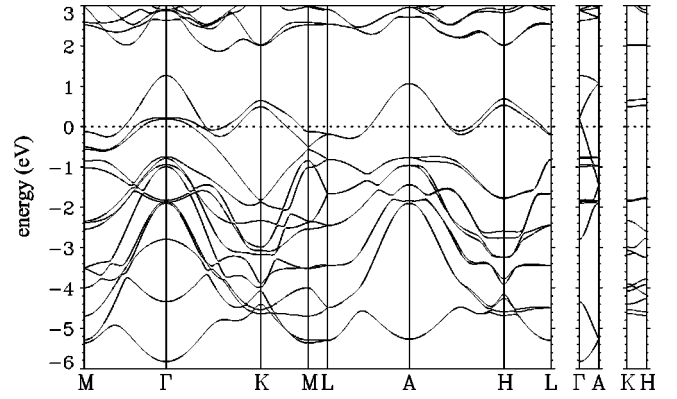
FIG. 1. Theoretical band structure of $2H$-NbSe$_2$ as obtained from the calculation along various high-symmetry directions in reciprocal space. The dashed line indicates the Fermi level.

50 K by sweeping the analyzer across the sample hemisphere and collecting only those photoelectrons that were excited from a relatively small (60 meV) energy window centered on the Fermi level E_F. This mapping technique was developed recently and was shown to provide direct images of the FS topology.[21,22] Note that the ARPES intensities are normalized to the photon flux and no further data manipulation, such as background correction or symmetrization has been applied. The apparent intensity modulations in equivalent parts of the BZ are mainly caused by matrix element effects.

Figure 2(a) shows the photoelectron intensity distribution $I(\mathbf{k}_\parallel, E_F)$ with $\mathbf{k}_\parallel$ denoting the surface-parallel electron wave vector. Apart from a slight variation of the surface-perpendicular wave-vector component $k_\perp$, this image closely corresponds to a horizontal cut through the BZ. It clearly reveals a hexagonal FS centered at $\Gamma(A)$ and a second sheet centered at $K(H)$, both of which are related to the Nb $4d$ bands. Though the double-walled nature of these two sheets is not directly observed by the mapping technique, it was shown before that the conduction band doublet is in fact resolvable by ARPES in the energy distribution curve (EDC) mode.[8] In contrast to the strong cylindrical FS features, the Se $4p_z$-derived pancake surface appears only as a slightly enhanced photoemission intensity in the center of the BZ—this being, nevertheless, the first indication of the FS pocket in an ARPES experiment.

For a more detailed view of the FS, we display the two-dimensional intensity gradient $|\nabla_{\mathbf{k}_\parallel} I|$ in Fig. 2(b). In addition, we include our band theoretical results in this figure for direct comparison. In systems with a flatband behavior, the maximum gradient of the photoemission intensity generally gives a more accurate estimate of the Fermi wave vector than the original intensity maximum,[23,24] though even the maximum gradient method may suffer from relative errors of up to 10% induced by matrix element effects.[25,26] As pointed out in Ref. 8, the maximum intensity and the maximum intensity gradient provide upper and lower bounds, respectively, for the inner sheet of the double-walled ΓA-centered FS cylinder. However, to give reliable estimates for both sheets of the cylinder, it is more appropriate to use the second intensity gradient maximum as an upper bound. This approach is corroborated by the fact that in Fig. 2(b) the

photoemission intensity　　　　max |gradient| + theory
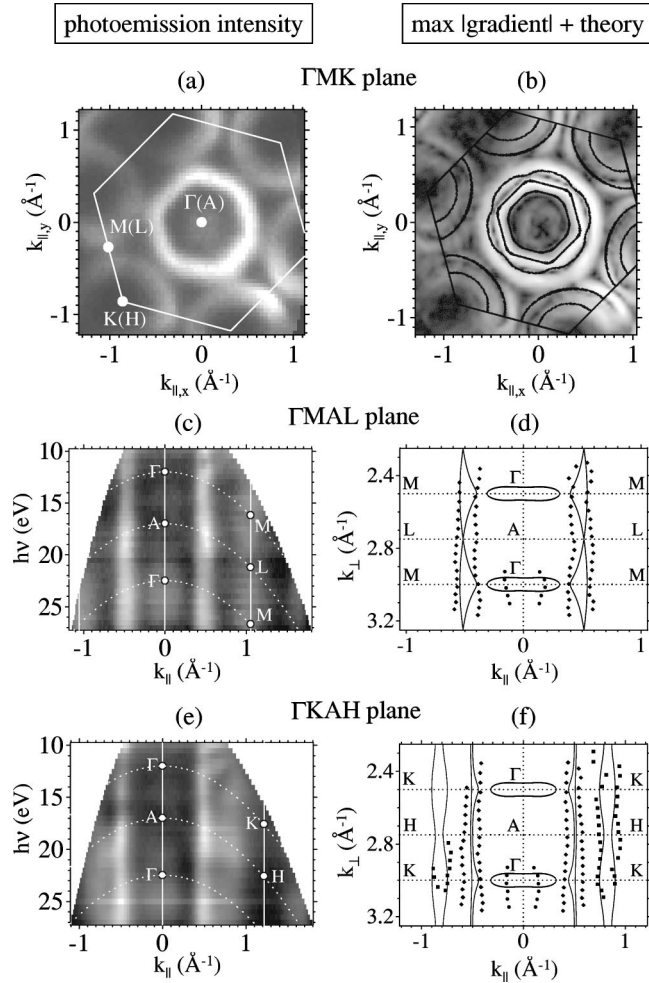
FIG. 2. Fermi-surface mapping of $2H$-NbSe$_2$ by ARPES at $T = 50$ K (left panel) and a theoretical Fermi surface obtained by bulk band-structure calculations (right panel). Panel (a) shows the $\mathbf{k}_\parallel$ distribution of the photoemission intensity measured at $h\nu = 24.5$ eV, and panel (b) shows the modulus of the two-dimensional intensity gradient in comparison with the calculated Fermi-surface cut at $k_\perp = 0$ [cf. Fig. 4(a)]. The $k_\perp$-dependent Fermi-surface mapping obtained by polar angle scans along the ΓM and ΓK directions of the Brillouin zone, recorded at $h\nu = 10$–27 eV, is given in (c) and (e). The dashed lines illustrate the $h\nu$ dependence of $k_\perp$ along the zone boundaries. Corresponding theoretical Fermi-surface cuts [(d) and (f)] are compared to the locations of the maximum photoemission intensity gradient (indicated by filled symbols). The respective $k_\perp$ values are determined assuming free-electron final states. In (a), (b), (c) and (e) the photoemission intensity is represented in a linear gray scale with white corresponding to high intensity. The Brillouin zone and the high-symmetry points are indicated.

theoretical double-walled Nb $4d$ FS's correspond very well to the bright contours (meaning a high modulus of the intensity gradient) of the gradient map. In contrast to cylindrical FS's, the measured pancake surface, which only shows up as a very weak ring in the center of the BZ, does not equally well correspond to the respective calculated FS: it appears to be clearly smaller in diameter than predicted by theory. Due to its blurred appearance, however, a correct interpretation of the pancake surface data is fairly difficult.

In order to reveal the $k_\perp$ dependence of the FS sheets, i.e., to reveal the three-dimensional character of the FS's, we have measured the photoemission intensity $I(\mathbf{k}_\parallel, E_F)$ as a function of the photon energy $h\nu$. To this end, we have performed polar angle scans along high-symmetry directions of the BZ for an appropriate range of polar emission angles and photon energies that span the bulk BZ cross sections. In Figs. 2(c) and 2(e) the resulting FS maps are shown in the ΓMAL and ΓKAH planes of the BZ. In both images, one can easily identify the cylindrical Nb $4d$-related FS sheet centered at the ΓA line and the Se $4p_z$-derived pocket at the Γ point. In addition, the KH cylinder is clearly resolved in Fig. 2(e), but it also leads to an enhanced intensity around the ML line in Fig. 2(c). The latter results from the low binding energy of the Nb $4d$-derived conduction band, which in this region is comparable to the width of the energy detection window.

For a comparison of experimental and theoretical band dispersions, we have determined the surface-perpendicular wave vector $k_\perp$ under the assumption of a free-electron final-state band. The best fit between the locations of maximum $|\nabla_{\mathbf{k}_\parallel}I|$ and the calculated bands was obtained when an inner potential of $V_0 = 17.6$ eV was used. As depicted in Figs. 2(d) and 2(f), the $k_\perp$ dependence of the maxima of the modulus of the ARPES intensity gradient reveals a high degree of two dimensionality for the Nb $4d$ FS cylinders—even higher than expected from the calculation. This deviation may be attributed to the fact that in these parts of the FS two nearby photoemission peaks of finite width are superimposed, leading only to a slight asymmetry of the resulting peak and a reduced dispersion of its edges, and that, additionally, matrix elements affect the locations of maximum $|\nabla_{\mathbf{k}_\parallel}I|$, as can be concluded from the photoemission intensity oscillations along the cylinders [see Figs. 2(c) and 2(e)]. Despite this discrepancy between experiment and theory, the maximum gradient analysis still provides good verification for the calculation, because the experimental data form excellent boundaries for the calculated double-walled Nb $4d$ cylinders over the entire BZ.

In contrast to cylindrical FS's, the experimentally determined pancake-shaped surface around the Γ point does not confirm the band theoretical results equally well. The experimental 'pancake' has a smaller $\mathbf{k}_\parallel$ extension, and does not appear as flat as predicted by theory. To improve the comparison, a more accurate mapping of the FS pocket would be needed. But this is rather complicated. As shown in Fig. 3(a), there is an overlap between the weak pancake structure and the much stronger signals from the FS cylinders which might be the reason why the FS pocket at the upper Γ point in Figs. 2(c) and 2(e) is not clearly resolved. More importantly, the $k_\perp$ extension of the pocket is comparable to the intrinsic $\mathbf{k}$-space uncertainty, which is primarily determined by the final-state lifetime, so that one cannot expect the corresponding photoemission peak simply to disappear upon crossing the Fermi level. The position of the peak maximum will rather become stationary near the Fermi energy, leading to just a small intensity decrease at E_F. In fact, we observe this behavior in Fig. 3(b), where the marked intensity drops can be attributed to the photoemission peak reaching the Γ point,
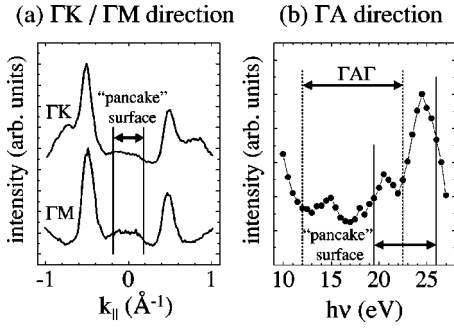
FIG. 3. Fermi-surface mapping of the pancake-shaped structure at the Γ point. We show the ARPES intensity at the Fermi level along the ΓK and ΓM directions (a) of the Brillouin zone ($h\nu$ = 22.5 eV) and photoemission intensity at E_F and $\mathbf{k}_\parallel = 0$ as a function of the photon energy (b). The approximate extensions of the Fermi-surface pocket are indicated by solid lines.

i.e., the point of maximum energy above E_F in the dispersion of the Se $4p_z$ state. Finally, Fig. 3(b) shows that any analysis of the experimental data is further complicated by fairly strong intensity variations due to matrix elements and the $h\nu$ dependence of the escape probability. As a consequence, the locations of maximum $|\nabla_{\mathbf{k}_\parallel} I|$ can only serve as rough estimates for the true dimensions of the FS pocket at the Γ point. For the same reason, even in the EDC mode of ARPES the correct Fermi level crossings of the Se $4p_z$-related band cannot be identified unambiguously.[27]

In conclusion, we find a good overall agreement between the experimental and theoretical FS topology of $2H$-NbSe$_2$, particularly for the Nb $4d$-derived cylinders. These parts of the FS are expected to be closely related to the CDW instability. Therefore, we address the CDW mechanism in $2H$-NbSe$_2$ in context of our theoretical results for the FS.

IV. CHARGE-DENSITY-WAVE MECHANISM

One of the key quantities in the theory of CDW instabilities is the wave-vector-dependent noninteracting electronic susceptibility $\chi_0(\mathbf{q})$, describing the gain that can be achieved in the one-electron band energy as a function of the wave vector $\mathbf{q}$.[28] For the $2H$ family of TMDC's, two alternative mechanisms have been proposed as to how $\chi_0(\mathbf{q})$ could be enhanced near $\mathbf{q}_{CDW}$, the wave vector of the observed CDW. Both of these rely on specific features of the electronic structure at or very close to the Fermi level. The well-known "nesting model" supposes that there are large parallel sections of the FS connected by the nesting vector $\mathbf{q}_0$ leading to a finite peak in $\chi_0(\mathbf{q})$ around $\mathbf{q}_0 = \mathbf{q}_{CDW}$. The height and shape of this peak are functions of the size and radii of curvature of the nested FS regions.[12–14] In the second model, suggested by Rice and Scott,[15] saddle points in a two-dimensional conduction band lying within a distance of $k_B T_{CDW}$ to the Fermi level are responsible for a logarithmic divergency in $\chi_0(\mathbf{q}_0)$, where $\mathbf{q}_0 = \mathbf{q}_{CDW}$ is now a wave vector connecting two saddle points. In both models one expects the FS to be gapped in the vicinity of its critical sections, i.e., the nested regions or the saddle points, respectively.

For the case of $2H$-NbSe$_2$, band-structure calculations,[7,9,10] including the one presented in this work, predict two-dimensional saddle points in the Nb $4d$-derived conduction-band doublet, indeed, at about $\frac{1}{2}\Gamma K$, but their binding energies are rather high [~ 100 meV for the band closer to the Fermi level according to our calculation (see Fig. 1)]. The saddle-point behavior near $\frac{1}{2}\Gamma K$ has been confirmed by recent ARPES results, and the experimentally determined binding energy of the saddle point in the higher conduction band even appears to be renormalized to < 50 meV.[8] Nevertheless, this energy is still large as compared to $k_B T_{CDW} \approx 3$ meV. In addition, neither the distance between two saddle-points measured along the ΓM direction of the BZ can account for the observed CDW, nor is a band energy lowering found around the saddle point in the CDW phase.[8] Therefore, it is most likely that the saddle point mechanism can be ruled out as an explanation of the CDW instability in $2H$-NbSe$_2$ on the basis of these results.

On the other hand, experimental results like those shown in Fig. 2(a) could easily be misconstrued as showing that the CDW transition in $2H$-NbSe$_2$ is driven by a self-nesting of the hexagonal ΓA-centered FS cylinder. Such an interpretation has to be contrasted with the fact, however, that both the size and the shape of this FS cylinder are not appropriate. From Fig. 2(d) we can directly read off $|\mathbf{q}_0| \geq 0.80$ Å^{-1} as an experimental *lower limit* and $|\mathbf{q}_0| \leq 1.20$ Å^{-1} as an experimental upper limit for the magnitude of the nesting vector along the ΓM direction of the BZ.[29] Our lower limit value is quite far off from the experimentally observed value of $|\mathbf{q}_{CDW}| = 0.688$ Å^{-1}. In addition, we find a considerable $k_\perp$ dispersion of the calculated FS cylinder, which does not yield the large parallel FS sheet necessary to produce a sharp peak in the electronic susceptibility.

In order to examine the nesting behavior in more detail, in Fig. 4 we show cuts of the calculated FS of $2H$-NbSe$_2$ for constant $k_\perp$ at three different $k_\perp$ values, and in each figure we include the cut obtained at the same $k_\perp$ value that includes a translation by the absolute value of the observed $\mathbf{q}_{CDW}$ (cf. Ref. 13) along the ΓM direction. Obviously, there is hardly any contribution to $\chi_0(\mathbf{q})$ arising from self-nesting of the ΓA-centered FS cylinder. Instead, the main contributions are associated with the inner KH cylinder, which nests with itself, as well as with its neighbor and with the inner ΓA cylinder. Due to the $k_\perp$ dispersion of the FS's, however, the overall nesting appears to be weak. This was already noted earlier,[12] and was quantitatively shown by calculations of the electronic susceptibility revealing no pronounced peaks but rather a broad hump in $\chi_0(\mathbf{q})$ around $\mathbf{q}_{CDW}$.[13,30] By sliding two copies of the FS cuts shown in Fig. 4 relative to each other, one can easily see how a broad maximum in $\chi_0(\mathbf{q})$ can occur, namely, because several FS features are brought near to nesting conditions in rapid succession. The important fact to note at this point is that the wave vector of the observed CDW of $2H$-NbSe$_2$ is not simply related to the FS geometry or, in other words, that the noninteracting *electronic* susceptibility $\chi_0(\mathbf{q})$ is not solely the dominant factor governing the CDW. Hence, for a comprehensive understanding of the CDW mechanism in $2H$-NbSe$_2$, detailed microscopic calcu-

(a) $k_\perp = 0$

(b) $k_\perp = \pi/2c$ (c) $k_\perp = \pi/c$
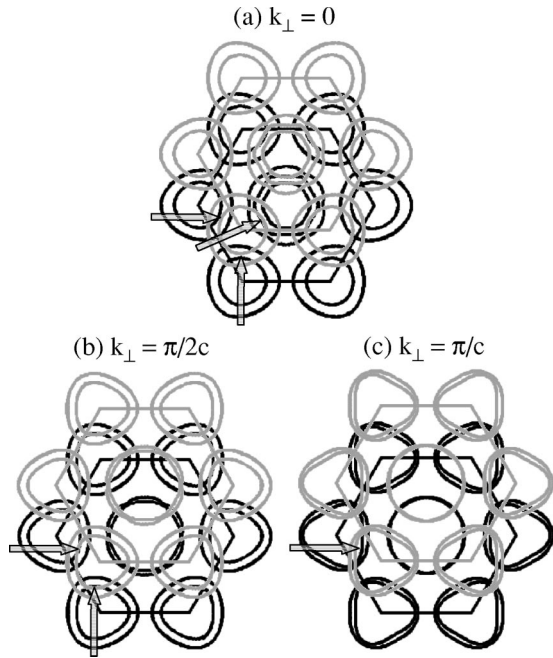
FIG. 4. Fermi-surface nesting for three different values of $k_\perp$: (a) $k_\perp = 0$, (b) $k_\perp = \pi/2c$, and (c) $k_\perp = \pi/c$. In each case, the grey Fermi surface cut is transfered by $\frac{2}{3}|\Gamma M|$, i.e., by the magnitude of the CDW wave vector, along the ΓM direction of the Brillouin zone. Nesting regions, which become quite obvious in the figure, are marked by arrows.

lations explicitly including electron-lattice interactions seem to be necessary.

As a consequence, one should not expect too much from drawing nesting vectors or from examining whether there are gaps opening up in the critical regions of the FS. The latter is anyway a critical task for 2*H*-NbSe$_2$ because of the small energy scale defined by the low onset temperature of the CDW $(k_B T_{CDW} \approx 3$ meV). In addition, resistivity[4] and heat-capacity[5] measurements indicate that the decrease in the density of states at the Fermi level associated with CDW formation is only of the order of 1%.

V. CONCLUSIONS

Our ARPES data on the CDW system 2*H*-NbSe$_2$ confirm the existence of all FS sheets predicted by band theory including a small pancake-shaped surface centered at the Γ point. We find, in particular, that Nb $4d$-related FS cylinders centered at the ΓA and KH lines of the BZ are in good correspondence with our fully relativistic *ab initio* band-structure calculation results. From the size and the $k_\perp$ dependence of the calculated FS sheets, we conclude that the wave vector of the CDW in 2*H*-NbSe$_2$ is not simply determined by the FS geometry. The observed weak FS nesting rather emphasizes the need for more detailed microscopic calculations including electron-phonon interactions to explain the CDW instability adequately. The required microscopic theory must go beyond the calculations presented in Refs. 13, 14, 30, and 31, where it has been shown that neither the electronic susceptibility $\chi_0(\mathbf{q})$ nor the $\mathbf{q}$ dependence of the electron-phonon matrix element can account for the observed CDW wave vector.

[1] R. Sooryakumar and M. V. Klein, Phys. Rev. Lett. **45**, 660 (1980).

[2] C.-H. Du, W. J. Lin, Y. Su, B. K. Tanner, P. D. Hatton, D. Casa, B. Keimer, J. P. Hill, C. S. Oglesby, and H. Hohl, J. Phys.: Condens. Matter **12**, 5361 (2000).

[3] D. E. Moncton, J. D. Axe, and F. J. DiSalvo, Phys. Rev. Lett. **34**, 734 (1975).

[4] J. R. Long, S. P. Bowen, and N. E. Lewis, Solid State Commun. **22**, 363 (1977).

[5] J. M. E. Harper, T. H. Geballe, and F. J. DiSalvo, Phys. Lett. A **54**, 27 (1975).

[6] J. E. Graebner and M. Robbins, Phys. Rev. Lett. **36**, 422 (1976).

[7] R. Corcoran, P. Meeson, Y. Onuki, P.-A. Probst, M. Springford, K. Takita, H. Harima, G. Y. Guo, and B. L. Gyorffy, J. Phys.: Condens. Matter **6**, 4479 (1994).

[8] Th. Straub, Th. Finteis, R. Claessen, P. Steiner, S. Hüfner, P. Blaha, C. S. Oglesby, and E. Bucher, Phys. Rev. Lett. **82**, 4504 (1999).

[9] L. F. Mattheiss, Phys. Rev. B **8**, 3719 (1973).

[10] G. Wexler and A. M. Woolley, J. Phys. C **9**, 1185 (1976).

[11] K. Takita, I. Umehara, T. Ebihara, N. Nagai, H. Nakashima, T. Kubota, H. Kondo, Y. Onuki, and S. Tanigawa, Physica C **185-189**, 2717 (1991).

[12] J. A. Wilson, Phys. Rev. B **15**, 5748 (1977).

[13] N. J. Doran, B. Ricco, M. Schreiber, D. Titterington, and G. Wexler, J. Phys. C **11**, 699 (1978).

[14] N. J. Doran, J. Phys. C **11**, L959 (1978).

[15] T. M. Rice and G. K. Scott, Phys. Rev. Lett. **35**, 120 (1975).

[16] K. Rossnagel, L. Kipp, M. Skibowski, and S. Harm, Nucl. Instrum. Methods Phys. Res. A **467-468**, 1485 (2001).

[17] P. Hohenberg and W. Kohn, Phys. Rev. **136**, B864 (1964).

[18] G. B. Bachelet, D. R. Hamann, and M. Schlüter, Phys. Rev. B **26**, 4199 (1982).

[19] D. M. Ceperley and B. J. Alder, Phys. Rev. Lett. **45**, 566 (1980).

[20] J. P. Perdew and A. Zunger, Phys. Rev. B **23**, 5048 (1981).

[21] A. Santoni, L. J. Terminello, F. J. Himpsel, and T. Takahashi, Appl. Phys. A: Solids Surf **52**, 229 (1991).

[22] P. Aebi, J. Osterwalder, P. Schwaller, L. Schlapbach, M. Shimoda, T. Mochiku, and K. Kadowaki, Phys. Rev. Lett. **72**, 2757 (1994).

[23] J. C. Campuzano, H. Ding, M. R. Norman, M. Randeria, A. F. Bellman, T. Yokoya, T. Takahashi, H. Katayama-Yoshida, T. Mochiku, and K. Kadowaki, Phys. Rev. B **53**, R14 737 (1996).

[24] Th. Straub, R. Claessen, P. Steiner, S. Hüfner, V. Eyert, K. Friemelt, and E. Bucher, Phys. Rev. B **55**, 13 473 (1997).

[25] L. Kipp, K. Rossnagel, C. Solterbeck, T. Strasser, W. Schattke,

and M. Skibowski, Phys. Rev. Lett. **83**, 5551 (1999).

[26] K. Rossnagel, L. Kipp, M. Skibowski, C. Solterbeck, T. Strasser, W. Schattke, D. Voss, P. Krüger, A. Mazur, and J. Pollmann, Phys. Rev. B **63**, 125104 (2001).

[27] This is inferred from normal and off-normal ARPES measurements in the EDC mode at various photon energies (unpublished).

[28] R. L. Withers and J. A. Wilson, J. Phys. C **19**, 4809 (1986).

[29] Our experimental lower limit is at variance with the one given in Ref. 8 ($|\mathbf{q}_0| \geqslant 0.69$ Å^{-1}) which was estimated from a less densely scanned intensity map [as compared to that shown in Fig. 2(b)], and thus might not be sufficiently accurate.

[30] K. Motizuki and E. Ando, J. Phys. Soc. Jpn. **52**, 2849 (1983).

[31] K. Motizuki, K. Kimura, E. Ando, and N. Suzuki, J. Phys. Soc. Jpn. **53**, 1078 (1984).